Chapter 11

Stress–Strain Models

Buddhism statue in Sukhothai, Thailand.

Sukhothai was the capital of the first Thai kingdom within the present territory of Thailand. Buddhism flourished in this capital. Sukhothai Kingdom reached its peak in late thirteenth Century under the reign of King Ramkhamhaeng. After him, however, Sukhothai declined quickly and came under control of Ayutthaya Dynasty in late fourteenth Century.

📖 11.1 Hyperbolic and Ramberg–Osgood Stress–Strain Models

Stress–strain relationship of soil is characterized by the rigidity when strain is small as well as the shear strength at large strains, which is the upper bound of the stress level. This fundamental nature of soil behavior has often been modeled by a hyperbolic curve (Fig. 11.1); refer to Kondner (1963) together with Kondner and Zelasko (1963).
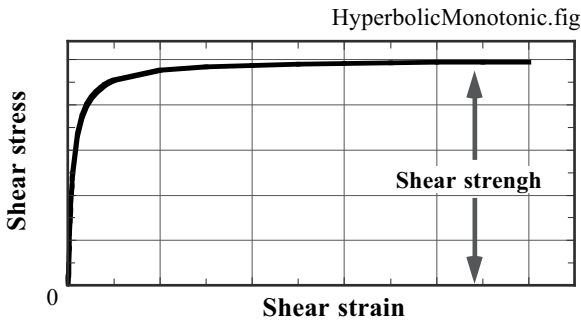
Fig. 11.1 Hyperbolic modeling of stress-strain behavior subjected to monotonic shear
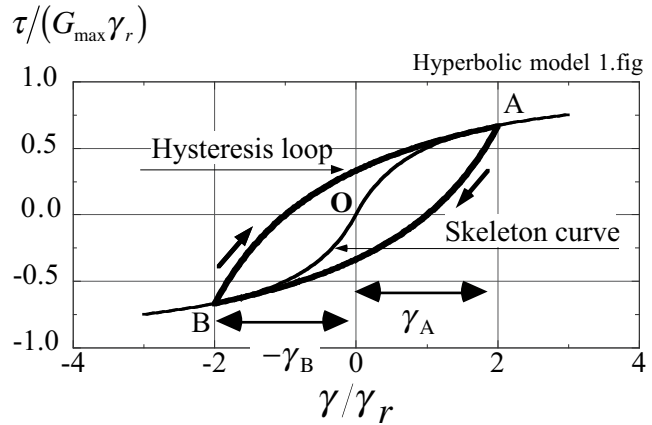
Fig. 11.2 Hyperbolic stress–strain model for cyclic loading

It is possible to model a cyclic stress–strain curve by a hyperbola as well. This model is used for dynamic analyses in the time domain. In case of *an analysis on a one-dimensional (level) ground subjected to horizontal shaking*,

$$\tau = \frac{G_{max}\gamma}{1+\left|\gamma/\gamma_r\right|},\qquad(11.1)$$

in which G_{max} is the shear modulus at a very small strain amplitude, while a parameter of γ_r is called the reference strain. Since

$$\tau \to G_{max}\gamma_r \quad \text{when} \quad \gamma \to \infty,$$

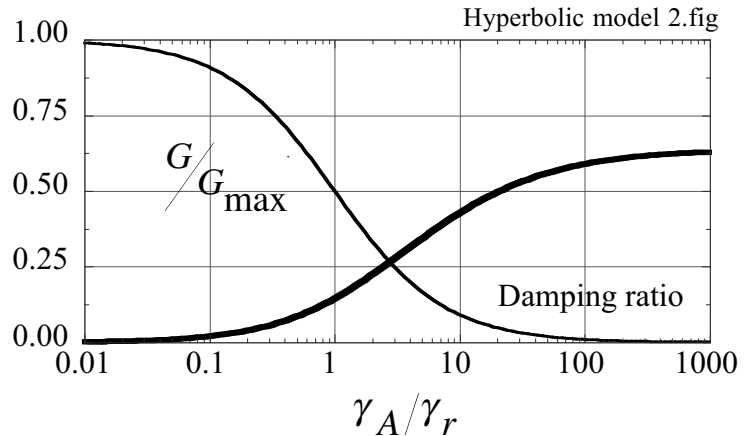γ_r stands somehow for shear strength property.

Fig. 11.3 G and h of hyperbolic model

The hyperbolic equation (11.1) models the skeleton curve BOA in Fig. 11.2. The skeleton curve is the one that passes through the ends of hysteresis loop with a variety of strain amplitude $\pm\gamma_A$ (Fig. 11.2). Equation (11.2) gives a formula for secant modulus, G, varying with the strain amplitude,

$$\frac{G}{G_{max}} = \frac{\tau/\gamma}{G_{max}} = \frac{1}{1+\left|\gamma_A/\gamma_r\right|}.\qquad(11.2)$$

The hysteresis loop, A⇒B⇒A in Fig. 11.2, is often modeled by enlarging the skeleton curve two times (Masing rule: Masing, 1926);

$$\frac{\tau-\tau_A}{2}=\frac{G_{max}\dfrac{\gamma-\gamma_A}{2}}{1+\left|(\gamma-\gamma_A)/(2\gamma_r)\right|}\quad\text{for A⇒B}\qquad\text{and}\qquad\frac{\tau-\tau_B}{2}=\frac{G_{max}\dfrac{\gamma-\gamma_B}{2}}{1+\left|(\gamma-\gamma_B)/(2\gamma_r)\right|}\quad\text{for B⇒A,}$$

where $\gamma_B = -\gamma_A$ and $\tau_B = -\tau_A$ as shown by (11.1). The damping ratio is obtained by calculating W and

ΔW (area of loop):

$$W = \frac{G\gamma_A^2}{2} = \frac{G_{max}\gamma_A^2}{2(1 + \gamma_A/\gamma_r)} \tag{11.3}$$

$$\Delta W = 2\int_{-\gamma_A}^{\gamma_A} (\text{Hysteresis loop B} \Rightarrow \text{A}) \, d\gamma = 2\int_{-\gamma_A}^{\gamma_A} \left\{ \tau_B + \frac{G_{max}(\gamma - \gamma_B)}{1 + |(\gamma - \gamma_B)/(2\gamma_r)|} \right\} d\gamma \tag{11.4}$$

$$= 2\int_{-\gamma_A}^{\gamma_A} \left\{ -\frac{G_{max}\gamma_A}{1 + \gamma_A/\gamma_r} + \frac{G_{max}(\gamma + \gamma_A)}{1 + (\gamma + \gamma_A)/(2\gamma_r)} \right\} d\gamma = \frac{4G_{max}}{1 + \gamma_A/\gamma_r} \frac{\gamma_A}{\gamma_r} \left(\frac{\gamma_A}{\gamma_r} + 2 \right) - 8G_{max}\gamma_r^2 \, \log_e\left(1 + \frac{\gamma_A}{\gamma_r} \right) \tag{11.5}$$

$$\text{Damping ratio, } h = \frac{2}{\pi}\left\{ \left(1 + \frac{2}{\gamma_A/\gamma_r} \right) - 2\frac{1 + \dfrac{\gamma_A}{\gamma_r}}{(\gamma_A/\gamma_r)^2} \, \log_e\left(1 + \frac{\gamma_A}{\gamma_r} \right) \right\} \tag{11.6}$$

Figure 11.3 demonstrates the relationship of G/G_{max} and h with the strain amplitude. It should be noted that the reference strain is the strain amplitude at which $G/G_{max} = 0.5$. The damping ratio at a very large strain amplitude approaches $2/\pi = 0.637$, which is much larger than what is reported by experiments (Chap. 10). Thus, the hyperbolic model should not be used in a large-strain range. Although its idea is clear, the hyperbolic model cannot freely adjust the shape of curves. Hence, experimental results cannot be fully considered. This problem is avoided in an equivalent-linear approach (Sect. 9.10) by using a model by Hardin and Drnevich (1972):

$$\text{Damping ratio, } h = \text{Maximum damping ratio at large strain} \times \left(1 - \frac{G}{G_{max}} \right)$$

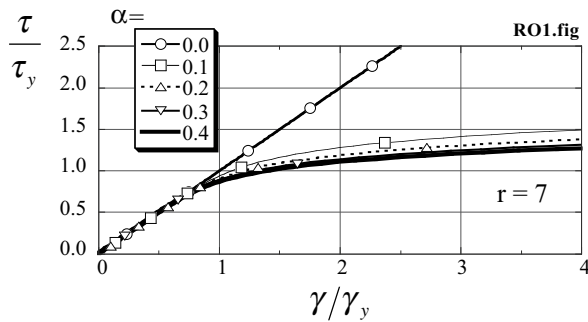in which G/G_{max} at a given strain amplitude is derived from (11.2).

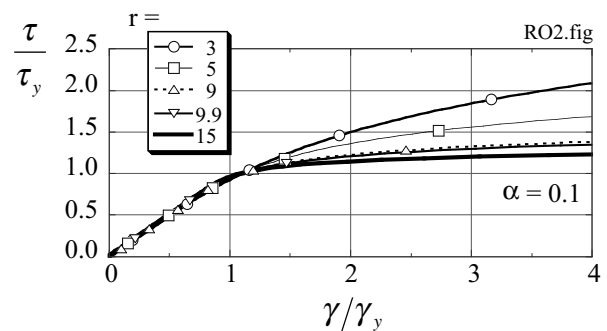**Fig. 11.4** Variation of skeleton curve with α **Fig. 11.5** Variation of skeleton curve with changing r.

The Ramberg–Osgood model is another kind of idea that reproduces the one-dimensional stress–strain behavior in the course of cyclic shear. Jennings (1964) used this model in terms of force and displacement. This text, however, describes the skeleton curve of this model by means of stress and strain:

$$\frac{\gamma}{\gamma_y} = \frac{\tau}{\tau_y}\left\{ 1 + \alpha\left(\frac{\tau}{\tau_y} \right)^{r-1} \right\} \tag{11.7}$$

in which a subscript "y" means characteristic values, while α and r are soil parameters to be determined by soil testing. Figures 11.4 and 11.5 illustrate the variation of curves by (11.7) with changing parameters:

The major features of this model as compared with the hyperbolic model are as what follows.

1. There is no upper bound in shear stress; i.e., $\lim_{\gamma \to \infty} \tau$ is infinite. Therefore, shear strength is not considered. As an alternative, soil parameters in the model are adjusted to make shear stress at 1% strain, for example, equal to an appropriate value.
2. Since there are three parameters, there is more freedom to take into account the complex soil behavior; for example, shear modulus at small strain, damping ratio at large strain, and shear stress at large strain.
3. Equation (11.7) helps calculate the strain value from a given value of stress. Shear stress, conversely, cannot be directly calculated from strain. This may make a nonlinear analysis more time consuming because stress determination needs iteration.

Both hyperbolic and Ramberg–Osgood models are intended to be used for a single-degree-of-freedom situation. Therefore, horizontal shaking of a level ground is their major target. Extension to a multi-dimensional situation needs more elaborate modeling.

📖 11.2 Dilatancy of Sand Subjected to Cyclic Drained Shear

Deformation of soil is characterized by dilatancy, which is the volume change induced by shear deformation (Sect. 1.6). Under cyclic loading, the volume change occurs as contraction, which means subsidence of ground surface after an earthquake event (Sect. 17.11). It will be shown later that the volume contraction in drained condition is equivalent with the development of excess pore water pressure in undrained conditions (Sect. 18.1). This is the cause of liquefaction and extensive damage.

Figure 11.6 illustrates an example of a drained cyclic shear test with a constant amplitude of strain conducted by a torsion shear apparatus (Sect. 18.8). The density of the tested sand was medium (relative density = 56%). It is first observed that the stress amplitude increases as the number of cyclic loading increases (see Fig. 10.6 as well). This implies that stiffness of soil increases with the progress of drained cyclic loading. Second, the net volumetric strain is contractive, accumulating toward 5% or more, although dilatant behavior is still observed when the shear strain exceeds 0.7%. Figure 11.7 illustrates more detailed variation of volumetric strain in one cycle in which both contraction and dilation occur in different phases of deformation.

(a) Stress–strain behavior
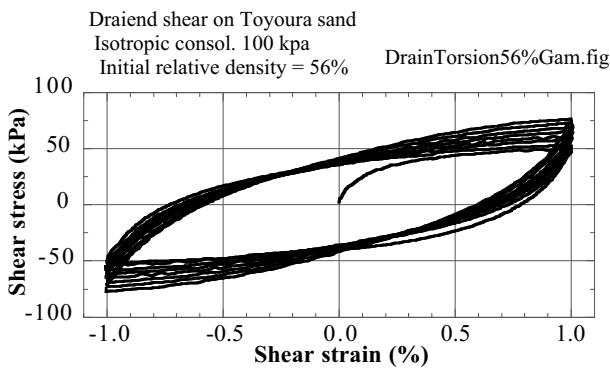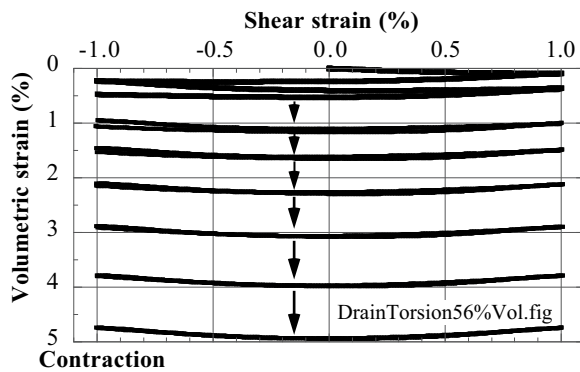

(b) Development of volume contraction

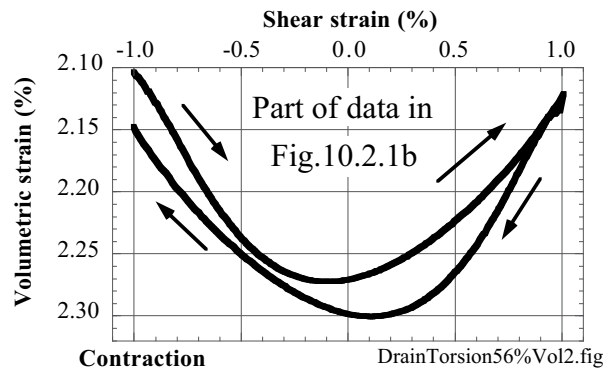**Fig. 11.6** Drained cyclic shear test (Dr = 56%)   (Shahnazari and Towhata, 2002)

Fig. 11.7 Accumulation of volumetric strain in one cycle of loading (data from Shahnazari and Towhata, 2002)
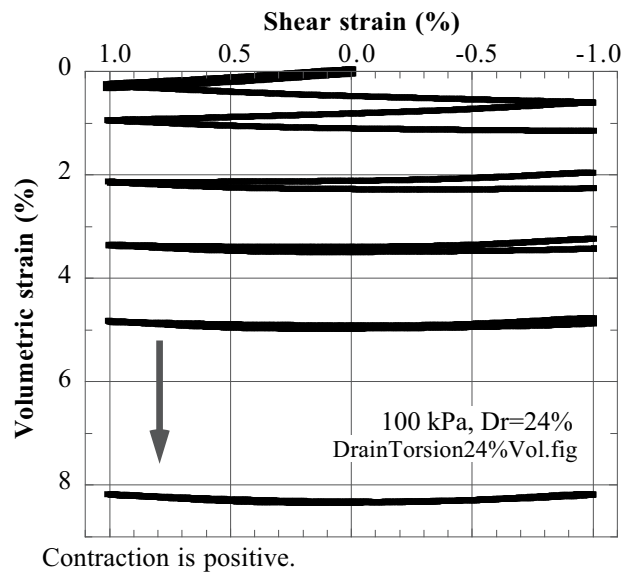

Contraction is positive.

Fig. 11.8 Volume change of very loose sand (Dr = 24%) (Shahnazari and Towhata, 2002)

Figure 11.8 indicates the volume contraction of looser sand. Although the consolidation stress and strain amplitude are identical with the data in Fig. 11.6, the accumulation of volume change occurred faster.

As mentioned in Sect. 1.6, the dilatant behavior of sand has been investigated by many people by using the so-called stress-dilatancy relationship:

$$\frac{\tau}{\sigma'} = K\left(-\frac{d\varepsilon_v}{d\gamma_p}\right) + \text{constant} \qquad (11.8)$$

in which ε_v designates the volumetric strain (positive in compression). Positive and negative dilatancy is reproduced in accordance with positive and negative values of $d\varepsilon_v/d\gamma_p$. Moreover, the present section employs γ_p, which is the plastic (irrecoverable) component of shear strain. The stress dilatancy relationship of sand undergoing cyclic loading was studied by Pradhan et al. (1989) and later by Hinokio et al. (2001). The present study, in contrast, attempts to indicate the stress-dilatancy behavior of sand subjected to more number of cycles.
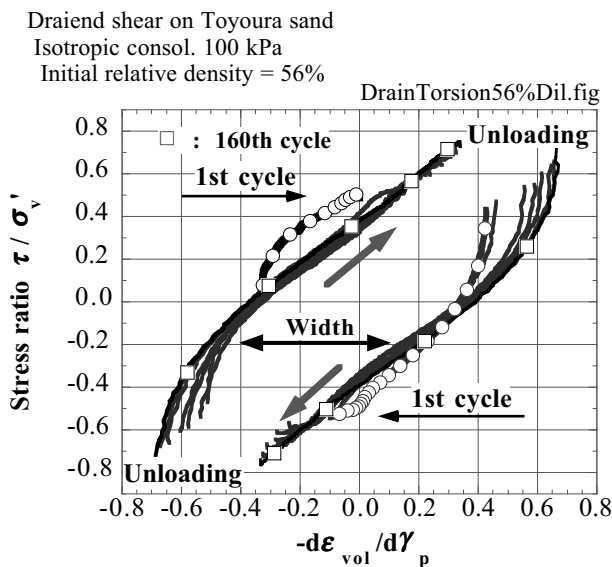

Fig. 11.9 Stress-dilatancy relationship of sand with relative density = 56% (Shahnazari and Towhata, 2002)
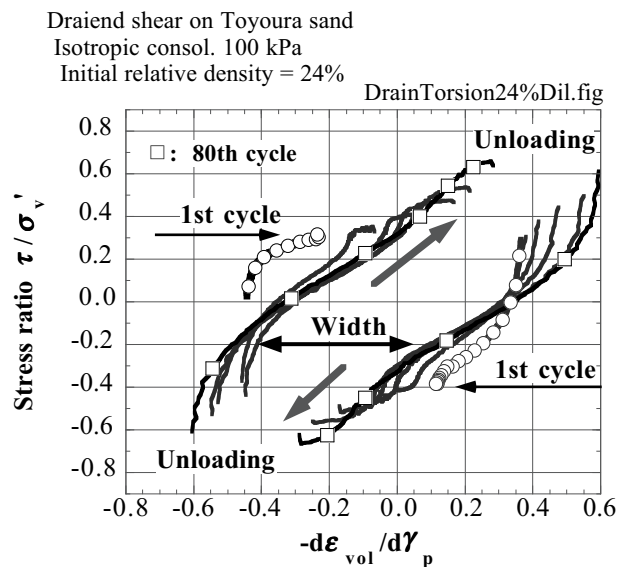

Fig. 11.10 Stress-dilatancy relationship of sand with relative density = 24% (Shahnazari and Towhata, 2002)

Figures 11.9 and 11.10 reveal two stress-dilatancy diagrams that were obtained by tests with relative densities of 56% and 24%, respectively. The employed number of loading cycles was 160 and 80, and the relative density was increased by cyclic loading to 80% and 69%, respectively. Only data from selected cycles was plotted in the figures. Note that $-d\varepsilon_{vol}/d\gamma_p < 0$ means volume contraction when the stress ratio, τ/σ_v', is increasing and vice versa. From these diagrams, the following points may be made:
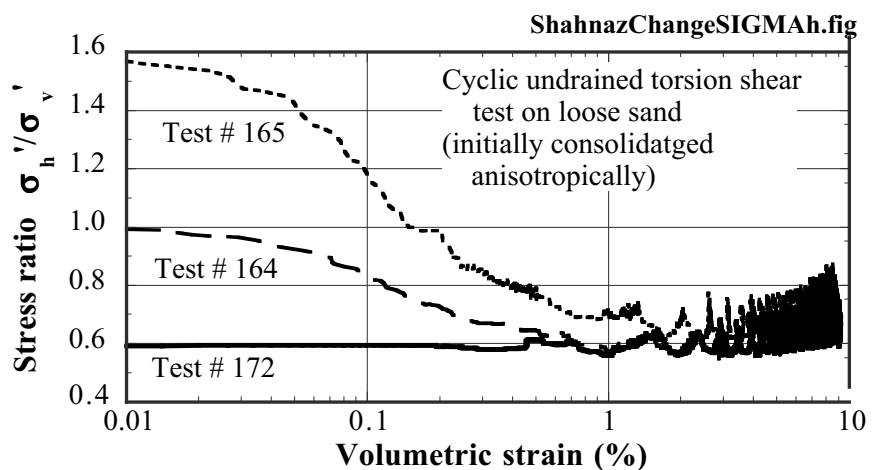

Fig. 11.11 Reduction of lateral earth pressure coefficient due to cyclic drained loading (Shahnazari and Towhata, 2002)

1. Although the density of sand affects the range of mobilized (activated) stress level, the range of dilatancy ratio, $-\mathrm{d}\varepsilon_{\mathrm{vol}}/\mathrm{d}\gamma_{\mathrm{p}}$, is not much affected.
2. There is an approximate linearity in the stress–dilatancy relationship.
3. $-\mathrm{d}\varepsilon_{\mathrm{vol}}/\mathrm{d}\gamma_{\mathrm{p}}$ jumps upon the initiation of unloading as reported by Pradhan et al. (1989).
4. The first cycle of loading exhibits greater values of $\left|-\mathrm{d}\varepsilon_{\mathrm{vol}}/\mathrm{d}\gamma_{\mathrm{p}}\right|$, which imply greater tendency for volume contraction.
5. Immediately after the onset of unloading (change of loading direction), $-d\varepsilon_{vol}/d\gamma_{p}$ exhibits volume contraction. This tendency increases as the number of loading cycles increases.
6. Conversely towards the end of loading (before unloading), $-\mathrm{d}\varepsilon_{\mathrm{vol}}/\mathrm{d}\gamma_{\mathrm{p}}$ shows greater values (more dilatancy), making the width of stress–dilatancy loop smaller; for definition of "width", see the figures.

Volume contraction as a consequence of cyclic shear results not only in ground subsidence but also in lateral contraction. In a horizontal ground where lateral strain is confined to zero, the potential contraction in the horizontal direction causes reduction of lateral earth pressure. Figure 11.11 is an experimental evidence of this phenomenon, which was obtained by torsion shear tests. This finding implies reduction of lateral earth pressure coefficient at rest (K_0).

📖 11.3 Theory of Elastoplasticity

Hyperbolic and Ramberg–Osgood models in Sect. 11.1 presented relationships between shear stress and strain, which are useful in dynamic analyses on horizontal ground. Since only one component of stress and one component of strain are therein studied, however, those models cannot be applied to two- or three-dimensional analyses in which many components of stress and strain are involved.

The elastoplastic modeling is one of the widely employed approaches to multi-dimensional modeling in which an increment of strain, $d\varepsilon$, induced by stress increments is decomposed into elastic and plastic components;

$$d\varepsilon = d\varepsilon^e + d\varepsilon^p \qquad (11.9)$$

where the prefix of "e" and the prefix of "p" designate elastic and plastic components, respectively. In the elastoplastic terminology, the elastic component is the one which is recovered upon removal of the loaded stress increments, while the plastic component remains unchanged (irreversible) upon unloading and reloading (Fig. 11.12). The elastic strain increments are calculated by a conventional elasticity framework. In a three-dimensional case, the isotropic theory of elasticity states
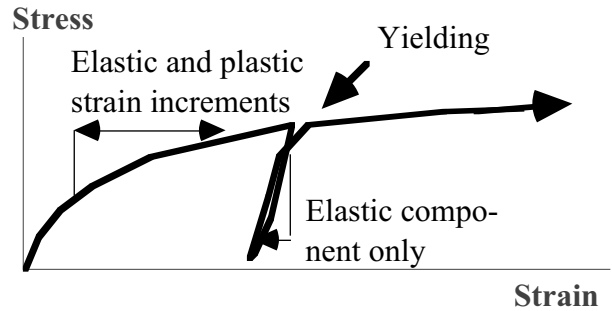
Fig. 11.12 Definition of elastic and plastic strain components

$$
\begin{Bmatrix} d\varepsilon_{xx} \\ d\varepsilon_{yy} \\ d\varepsilon_{zz} \\ d\gamma_{xy} \\ d\gamma_{yz} \\ d\gamma_{zx} \end{Bmatrix}^e
= \frac{1}{E}
\begin{bmatrix}
1 & -v & -v & 0 & 0 & 0 \\
-v & 1 & -v & 0 & 0 & 0 \\
-v & -v & 1 & 0 & 0 & 0 \\
0 & 0 & 0 & 2(1+v) & 0 & 0 \\
0 & 0 & 0 & 0 & 2(1+v) & 0 \\
0 & 0 & 0 & 0 & 0 & 2(1+v)
\end{bmatrix}
\begin{Bmatrix} d\sigma_{xx} \\ d\sigma_{yy} \\ d\sigma_{zz} \\ d\tau_{xy} \\ d\tau_{yz} \\ d\tau_{zx} \end{Bmatrix}^e
\qquad (11.10)
$$

in which E is the Young's modulus (modulus of elasticity), v is the Poisson ratio, and $E/\{2(1+v)\}$ is often called the shear modulus, G. In case that stress–strain relationship is nonlinear, these soil parameters are defined by tangent values and change with the magnitudes of stress components, void ratio, and possibly other soil parameters.

The theory of plasticity prefers to use the tensor way of designation for stress and strain. The relationships between the tensor designation and the engineering designation (11.10) are given by

$$
\begin{aligned}
&\{\varepsilon_{11} \quad \varepsilon_{22} \quad \varepsilon_{33} \quad \varepsilon_{12} \quad \varepsilon_{21} \quad \varepsilon_{23} \quad \varepsilon_{32} \quad \varepsilon_{31} \quad \varepsilon_{13}\} \\
&= \{\varepsilon_{xx} \quad \varepsilon_{yy} \quad \varepsilon_{zz} \quad \gamma_{xy}/2 \quad \gamma_{xy}/2 \quad \gamma_{yz}/2 \quad \gamma_{yz}/2 \quad \gamma_{zx}/2 \quad \gamma_{zx}/2\},
\end{aligned}
\qquad (11.11)
$$

$$
\begin{aligned}
&\{\sigma_{11} \quad \sigma_{22} \quad \sigma_{33} \quad \sigma_{12} \quad \sigma_{21} \quad \sigma_{23} \quad \sigma_{32} \quad \sigma_{31} \quad \sigma_{13}\} \\
&= \{\sigma_{xx} \quad \sigma_{yy} \quad \sigma_{zz} \quad \tau_{xy} \quad \tau_{xy} \quad \tau_{yz} \quad \tau_{yz} \quad \tau_{zx} \quad \tau_{zx}\}.
\end{aligned}
\qquad (11.12)
$$

By using the tensor designations, the theory of plasticity (Hill, 1983) expresses increments of plastic strain as

$$d\varepsilon_{ij}^{p} = h \frac{\partial g}{\partial \sigma_{ij}} \, df \quad (i,j = 1,2,3) \qquad (11.13)$$

in which h, g, and f are called hardening function, plastic potential, and yield function, which are functions of stress components and soil density possibly together with other soil parameters.

The theory of plasticity has several hypotheses. First, the plastic deformation occurs only when the yield function, f, increases. In other words, plastic deformation occurs only after yielding (Fig. 11.12) and no plastic deformation occurs when the current stress level is lower than the previous maximum value. In the extreme case where deformation is large close to failure, the yield function becomes similar to a failure criterion (Sect. 1.5).

Second, the ratio of components in a plastic strain increment (11.13) is independent of the magnitude and direction of stress increment. In other words, the orientation of the vector of plastic strain increment in Fig. 11.13 is independent of the direction and magnitude of the stress increment vector. This orientation is determined (flow rule) by partial derivative of the plastic potential function, $\partial g/\partial \sigma_{ij}$. Hence, this orientation is normal to the plane of constant g function. The stress–dilatancy relationship (Sect. 1.6) that is widely observed in soil testing determines the ratio of shear and volumetric strains and therefore is a kind of flow rule (Fig. 11.14).
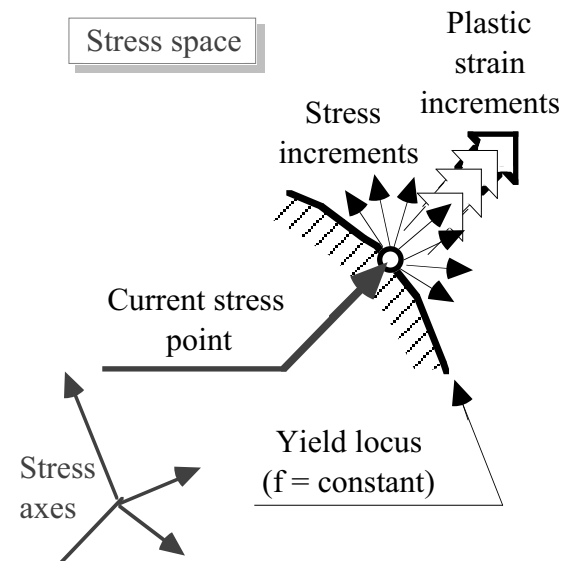

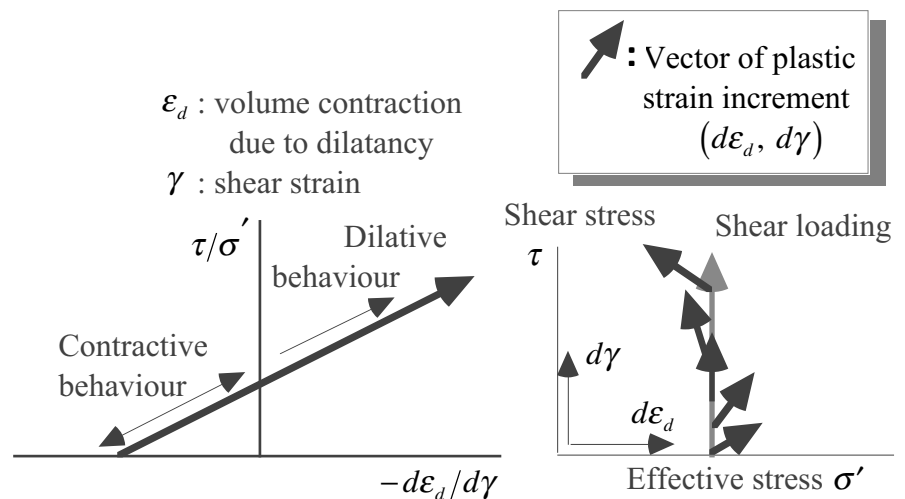**Fig. 11.13** Schematic illustration of plastic strain increments

Fig. 11.14 Use of stress-dilatancy relationship as flow rule of plasticity

Some theories employ g that is equal to f (associated flow rule). In this situation, the vector of plastic strain increment is normal to the yield locus (Fig. 11.13). This feature is called normality. On the contrary, the nonassociated flow rule employs different f and g functions.

The magnitude of the plastic strain increment vector is determined by the increment of the yield function, $df = \left(\partial f/\partial \sigma_{ij}\right)d\sigma_{ij}$, in (11.13).

Principal stresses (Sect. 1.3) play a major role in plasticity theory. The requirement of objectivity states that the ground deformation as calculated by the plasticity theory has to be independent of the choice of coordinate directions (x-y-z system or x'-y'-z' system). Therefore, h, g, and f functions in (11.13) are functions of principal stresses that are independent of the coordinate system. In other words, they are functions of stress invariants such as

$$\left(\sigma_1' + \sigma_2' + \sigma_3'\right)/3, \ \left(\sigma_1' - \sigma_2'\right)^2 + \left(\sigma_2' - \sigma_3'\right)^2 + \left(\sigma_3' - \sigma_1'\right)^2, \text{ and } \sigma_1' \times \sigma_2' \times \sigma_3'.$$

Effective stress components are used in the above expression because soil behavior is governed not by the total stress but by the effective stress. The third hypothesis of plasticity theory is called coaxiality, which states that the principal axes of stress and plastic strain increments are parallel to each other (Fig. 11.15).
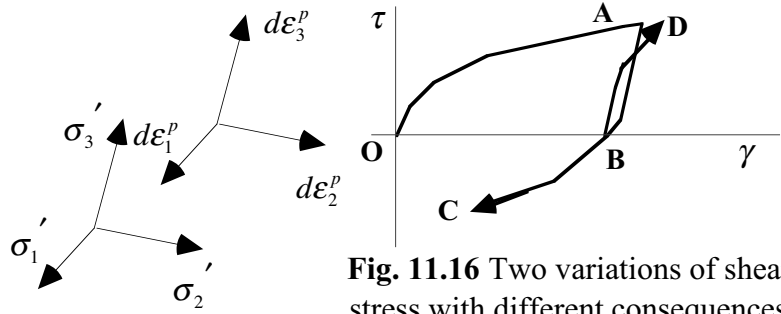
Fig. 11.15 Conceptual drawing of coaxiality

Fig. 11.16 Two variations of shear stress with different consequences

The use of principal stresses or stress invariants in functions h, g, and f causes one significant problem in application of plasticity theory to cyclic stress history. Figure 11.16 compares two kinds of shear stress history: OABC and OABD. Since the principal stress formulation cannot recognize the different direction of shear stress after B, continued soft behavior in BC and elastic reloading in BD cannot be reproduced. This problem is significant in the popular P'-q formulation $\left[P' = \left(\sigma_1' + \sigma_2' + \sigma_3'\right)/3 \text{ and } q = \sigma_1' - \sigma_3'\right]$ as well.
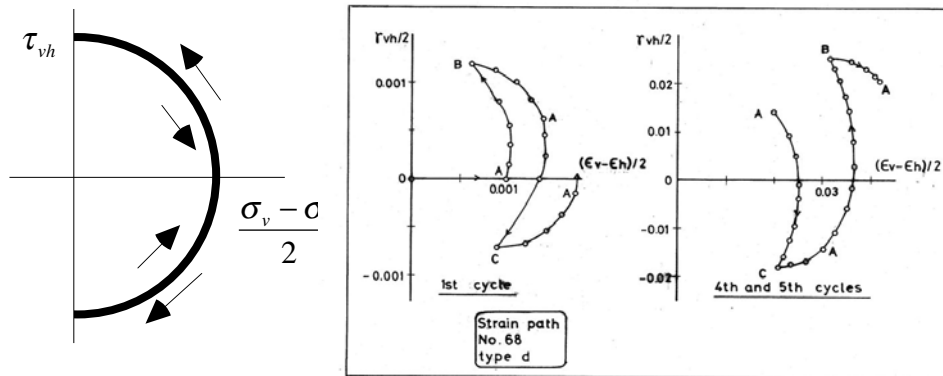
Fig. 11.17 Development of plastic shear strain under continuous rotation of principal stress axes

It is physically possible that principal stress axes rotate significantly while maintaining the magnitudes of σ_1', σ_2', and σ_3' constant. Since f, g, and h functions are held constant under constant values of principal stresses, the theory of plasticity does not give plastic stress increments; $df = 0$ in (11.13). In reality, on the contrary, such stress components as τ_{xz} can still vary, and changes corresponding strain components (γ_{xz} for example). Consequently, plastic strain of γ_{xz}^P can develop (Ishihara and Towhata, 1983). Figure 11.17 illustrates the development of shear strains, $\left(\varepsilon_v - \varepsilon_h\right)/2$ and γ_{vh}, undergoing cyclic rotation of principal stress axes while maintaining $\sigma_1 - \sigma_3$ constant. Figure 11.18 shows vectors of strain increments along another circular stress path. As the stress state approached failure in the third cycle, the vector became greater and more perpendicular to the circular stress path. Thus, the strain increment vector became overwhelmed by plastic components that were coaxial with the principal stress.

Consequently, it is reasonable to state that elastoplasticity theory for, in particular, complex cyclic loading should be formulated with special provisions for stress axes rotation; simple use of stress invariants is not appropriate. An example of such a provision is the use of stress difference tensor,

$\sigma_{ij} - \sigma_{ij}*$, in which $\sigma_{ij}*$ stands for the stress state at the beginning of unloading (Point A in Fig. 11.16). This kind of modeling produces plasticity mechanism even when the stress level decreases from the previous maximum value (inside the yield locus in the classical sense) as schematically illustrated in Fig. 11.19. Mroz et al. (1978) developed such a theory.
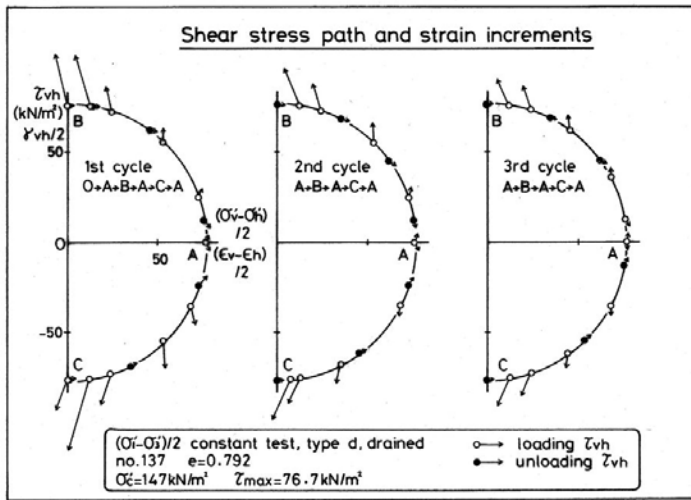

Fig. 11.18 Development of strain increments during continuous rotation of principal stress axes
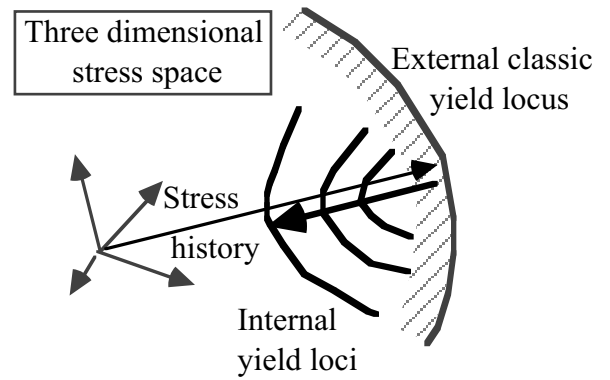
Fig. 11.19 Idea of multiple yield mechanisms of plasticity

📖 11.4 Dilatancy under Cyclic Loading

Dilatancy is a phenomenon of volume change caused by shear deformation of discrete material (Sects. 1.2 and 1.6). In earthquake engineering practice, volume contraction due to dilatancy (negative dilatancy) is important because it stands for ground subsidence induced by strong shaking. Dilatancy plays an extremely important role in liquefaction analysis (Chap. 2) as well, because the major cause of liquefaction and large ground deformation is the development of high pore water pressure caused by dilatancy (Sect. 18.1).
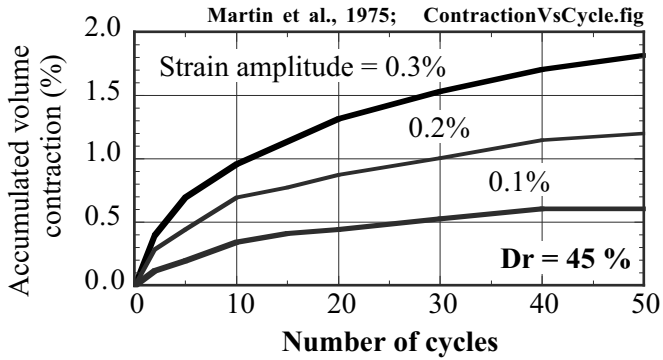

Fig. 11.20 Volume contraction of sand due to cyclic shear (Martin et al., 1975)
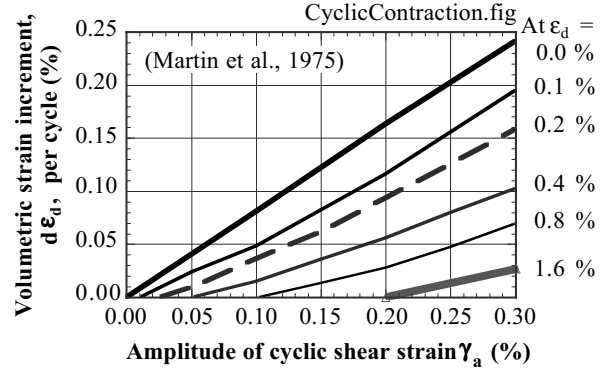

Fig. 11.21 Increment of volumetric strain per cycle of shear strain (Martin et al., 1975)

This section concerns modeling of dilatancy under one-dimensional cyclic shear loading. There are two kinds of approach for modeling of dilatancy. One is modeling of volume change, which is measured in cyclic drained shear of sand. Martin et al. (1975) conducted drained cyclic simple shear tests and reported that the volumetric strain due to dilatancy is proportional to shear strain amplitude; see Fig. 11.20. They studied the increment of volumetric strain per cycle (Fig. 11.21) and proposed an empirical formula,

Fig. 11.22 Stress-path model of dilatancy and excess pore water pressure (see Set. 22.4)

$$\mathrm{d}\varepsilon_{\mathrm{d}} = C_1\left(\gamma_{\mathrm{a}} - C_2\varepsilon_{\mathrm{d}}\right) + \frac{C_3\varepsilon_{\mathrm{d}}^{\,2}}{\gamma_{\mathrm{a}} + C_4\varepsilon_{\mathrm{d}}}, \quad (11.14)$$

where $\mathrm{d}\varepsilon_{\mathrm{d}}$ is the increment of volumetric strain per cycle of strain amplitude γ_{a}. If cyclic loading occurs in a drained manner (dry sand for example), this ε_{d} is equal to the real volume compression. If loading is undrained as is the case of liquefaction, this potential volume contraction is converted to the decrease in effective stress under constant volume by

$$\mathrm{d}\sigma' = K\left(\mathrm{d}\varepsilon_{\mathrm{v}} - \mathrm{d}\varepsilon_{\mathrm{d}}\right), \qquad (11.15)$$

where ε_{v} is the volumetric strain that does occur in reality. Note that $\varepsilon_{\mathrm{v}} = 0$ under perfectly undrained conditions. Moreover, K is called bulk modulus of soil and is equivalent with $1/m_{\mathrm{v}}$ (m_{v} being volume compressibility in (1.12)) in consolidation theory. The determination of soil parameters in (11.14) requires cyclic drained loading on undisturbed soil specimens.
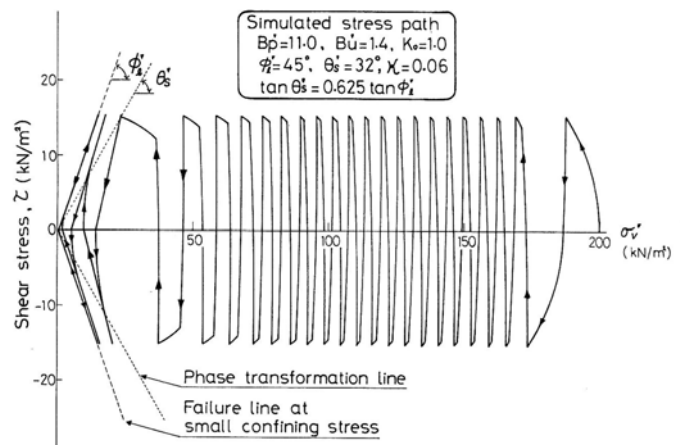
The other approach to modeling of dilatancy is that of excess pore water pressure that develops during undrained cyclic loading. Apparently, this approach is related with liquefaction tests on sand. Figure 11.22 (Ishihara and Towhata, 1982) indicates a modeled relationship between decrease in effective stress (increase in pore water pressure) and cyclic change in shear stress. This stress path model consists of three parts: under loading (increase of shear stress), unloading (decrease of shear stress), and that near perfect liquefaction.

Both approaches as described above concern one-dimensional cyclic loading (case of horizontal ground subjected to one direction, EW or NS, of shaking). For more complicated situations, those models have to be significantly revised, or more complicated models such as stress–dilatancy approach of plasticity (Sects. 1.6 and 11.3) for volume change or energy correlation of pore water pressure (Sect. 20.8–20.10) are employed.

📖 11.5 Multi-Nonlinear Spring Model

Figure 11.23 illustrates an example of multi–nonlinear spring model for a two-dimensional situation in which simultaneous loading of $(\sigma_v - \sigma_h)/2$ and τ_{vh} associated with continuous rotation of principal stress axes is taken into account (Towhata and Ishihara, 1985). The big arrow in the figure stands for the above-mentioned shear stress components and its variation induces the displacement of the point of action at the center. This displacement stands for the shear strain of soil; $(\varepsilon_v - \varepsilon_h)/2$ and $\gamma_{vh}/2$. Note that the ratio of two stress components (direction of the arrow) indicates the orientation of principal stresses. When this orientation rotates, the direction of

Fig. 11.23 Multi-spring model for two-dimensional shear deformation

the arrow changes and component springs are subjected to nonlinear deformation. Consequently, plastic deformation is produced. This model was combined with the energy correlation of excess pore water pressure (Sects. 20.8–20.10) to reproduce the undrained cyclic behavior of loose sand. It was applied by Iai et al. (1992a,b) to develop a seismic design code of harbor structures.
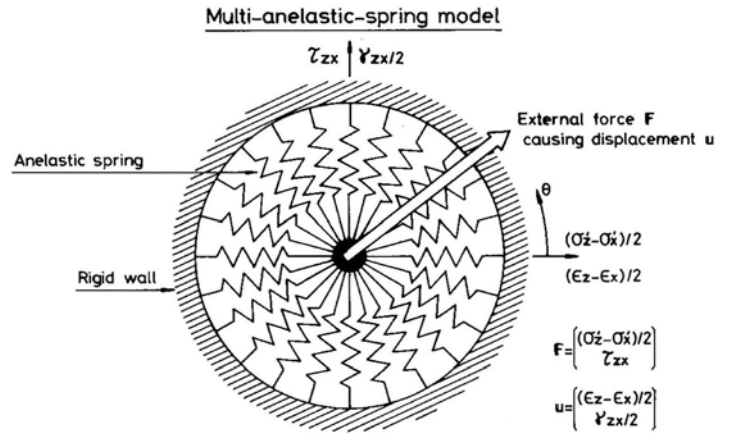
The relationship between the nature of springs and the reproduced soil properties are as what follows. In an ideal case where the number of springs is infinite, the shear modulus of soil at small strain, G_{max}, and the spring modulus at small deformation, $k_{max}d\theta$, are related to each other by supposing a loading in the direction of $\pi/2$ in Fig. 11.23;

$$G_{max} = \int_{\pi/2}^{5\pi/2} k_{max}\left\{\cos\left(\theta - \frac{\pi}{2}\right)\right\}^2 \, d\theta = \pi k_{max}. \qquad (11.16)$$

When the deformation of springs is extremely large, all the springs develop their full strength; $F_f \, d\theta$. Accordingly, the magnitude of shear strength of modeled soil is given by

$$\text{Shear strength of soil} = 2\int_0^{\pi} F_f \, \cos\left(\theta - \frac{\pi}{2}\right) d\theta = 4F_f. \qquad (11.17)$$

These simple calculations assumed that all the springs have identical properties of k_{max} and F_f. By changing these parameters with the direction of springs, θ, it is possible to model anisotropic soil properties.

Since a two-dimensional condition has two independent shear stress components such as $(\varepsilon_z - \varepsilon_x)/2$ and γ_{zx} or γ_x and γ_y, the two-dimensional model illustrated in Fig. 11.23 is useful. In a three-dimensional condition, there are five independent shear stresses (six stresses minus mean effective stress) and its modeling by a multi-spring model is not easy. Simple expansion of the circle in the figure to a three-dimensional sphere is not sufficient because a sphere can handle only three degrees of freedom. Nishimura and Towhata (2004) solved this problem by allocating many circle models on the surface of a sphere; two degrees of freedom from a circle and three more degrees from the sphere.

It seems promising to extend the stress–dilatancy relationship (Fig. 11.14) to a multi-dimensional conditions. This goal may be achieved by employing the generalized shear stress of $\tau \equiv$

$\sqrt{\dfrac{3}{2}\left(\sigma'_{ij} - \delta_{ij}\sigma'_{m}\right)\left(\sigma'_{ij} - \delta_{ij}\sigma'_{m}\right)}$ and the generalized shear strain of $\gamma \equiv \sqrt{\dfrac{2}{3}\left(\varepsilon_{ij} - \dfrac{\delta_{ij}\varepsilon_{v}}{3}\right)\left(\varepsilon_{ij} - \dfrac{\delta_{ij}\varepsilon_{v}}{3}\right)}$. In

these expressions, i and j are 1, 2, or 3, while δ_{ij} stands for the Kronecke's delta;

$\delta_{ij} = 1$ if $i = j$ and $\delta_{ij} = 0$ if $i \neq j$.

Moreover, $\sigma'_{m} \equiv \left(\sigma'_1 + \sigma'_2 + \sigma'_3\right)/3$ designates the effective mean principal stress, and ε_{v} is the volumetric strain. Note that the above definitions of τ and γ follow the tensor abbreviation;

$A_k B_k \equiv \sum\limits_k A_k B_k$ and, in particular, $\tau_{ij}\tau_{ij} \equiv \sum\limits_i \sum\limits_j \tau_{ij}\tau_{ij}$

The problem lying in the stress–dilatancy formulation is that no volumetric strain occurs if cyclic loading occurs with a constant value of γ; if $d\gamma = 0$, $d\varepsilon_{v}$ has to be zero in order to avoid an infinite value of $d\varepsilon_{v}/d\gamma$.

The bowl model was proposed by Fukutake and Matsuoka (1989) with a scope to predict volume contraction of sand undergoing multi-dimensional cyclic shear. For illustration, this section studies a situation of Fig. 11.24 where soil is sheared by two components of shear stress: τ_x and τ_y. The associating shear strains, γ_x and γ_y, are substituted in the dilatancy model in Fig. 11.25 where a bowl-like curved surface stands for the relationship between volume change and shear strain. The concave shape stands for the fact that volume expands when shear strain is large. See its similarity with the experimental curve in Fig. 11.8.
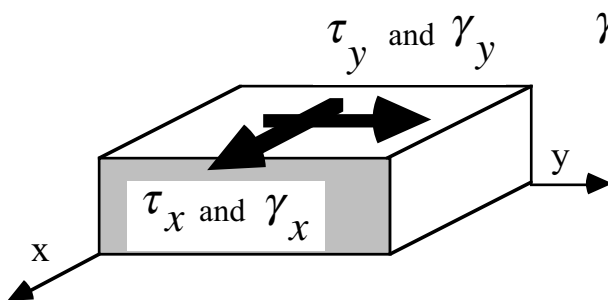

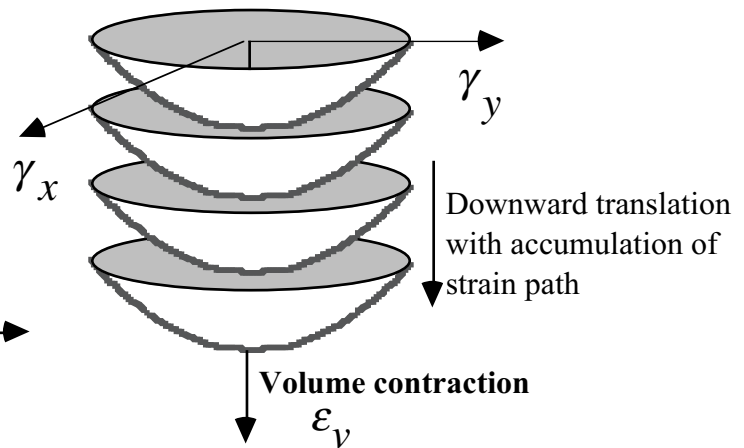
Fig. 11.24 Soil subjected to two-dimensional shear

Fig. 11.25 Conceptual illustration of bowl model of dilatancy

Since the volume of soil further continues to contract with the number of shear cycles, the bowl surface moves down in Fig. 11.25, thus representing the accumulated volumetric contraction during cyclic loading. This downward translation is a function of the shear strain path;

Length of shear strain path $\equiv \int\left[\left(d\gamma_x\right)^2 + \left(d\gamma_y\right)^2\right]$.

☀ 11.6 Discrete Element Analysis

Although the finite element analysis has been proved to be a powerful tool to calculate deformation of a continuous medium, there have been different attempts that consider materials discontinuous. This attempt is appropriate for such situations as post-failure behavior of rock slopes in which blocks of breached rock move and collide independently (Cundall, 1971; Kawai and Takeuchi, 1981).

Deformation analysis on an assembly of circular or spherical objects started in 1950s (Deresievicz, 1958a,b). Since sand consists of grains, this approach is attractive; particularly being so when displacement is large. Hence, a method of analysis called distinct element analysis or discrete element analysis (DEM) has been developed in which particles move and collide with each other (Cundall and Strack, 1979). However, the limited capacity of computers has not allowed to analyze behavior of real individual grains in either two-dimensional or three-dimensional manners; the number of real grains is too many for any computer memory. Hence, the existing DEM works in a two-dimensional manner on imaginary grains, which are much bigger than real grains. The two-dimensional analysis employs void ratio, which is smaller than the well-known void ratio range in real sandy deposit. For example, a regular packing of round grains in Fig. 11.26 has void ratio of $1-\pi/4 = 0.273$.
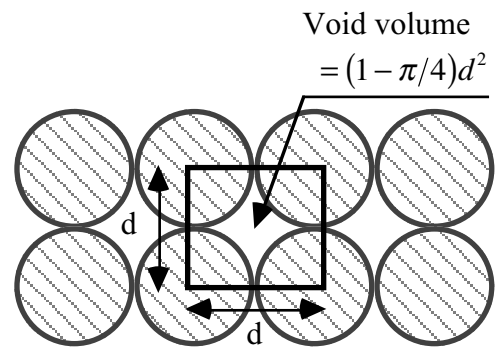

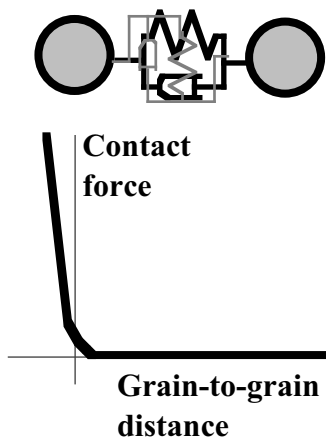**Fig. 11.26** Regular packing of two-dimensional circular grains

Void volume $= (1-\pi/4)d^2$

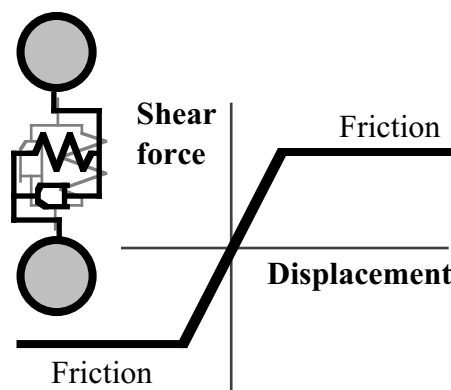**Fig. 11.27** Contact mechanism in normal direction

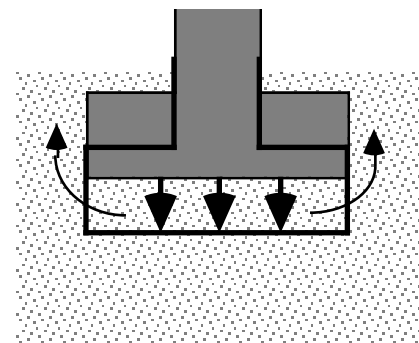**Fig. 11.28** Contact mechanism in shear direction

Fig. 11.29 Grains turning around corner

In DEM, the grain-to-grain interaction is modeled by nonlinear springs and dashpots, which are illustrated in Figs. 11.27 and 11.28. When the grain-to-grain distance is short, a particle contact occurs, and a normal mechanism (Fig. 11.27) is activated to resist against compression. At the same time, a shear resistant mechanism (Fig. 11.28) is generated that stands for friction between grains. The magnitude of friction in Fig. 11.28 varies with the extent of contact force in Fig. 11.27. DEM analysis is more advantageous than FEM when displacement and deformation are large. For example, DEM can calculate grain movements that turn around a corner of sinking foundation (Fig. 11.29), while such an analysis is very difficult in FEM.

In a dynamic analysis, the grain-to-grain distance has to be examined for pairs of extremely many particles at every time increment. To make ease this procedure, most DEM analyses employ circular or spherical grains. Moreover, previous DEM assumed only such two types of mechanisms as compression and shear at contact points. This idea is reasonable when the real contact occurs at a single point. If the real contact occurs by a plane or two points, the transfer of moment becomes important. Iwashita and Oda (1998) installed bending moment mechanism at contacts of imaginary spherical particles.

For an application to geotechnical earthquake problems, Kanatani et al. (2001) combined FEM and DEM in which FEM was applied to a more continuous soil deposit, while DEM to an accumulation of big concrete pieces. Furthermore, Hakuno and Tarumi (1988) as well as Nakase et al. (1998) showed how to calculate excess pore water pressure and seepage flow in a water-saturated model. Figure 11.30 illustrates an example calculation of liquefaction-induced deformation in a 30*g* centrifuge test. The number of spherical elements are 14,000 with the diameter of 0.4 mm. Shaking of 300 Gal with 2 Hz was applied. It is seen in this figure that the subsidence was terminated after some subsidence at which the buoyancy and gravity forces achieved equilibrium. Note that the force equilibrium after some displacement can be reproduced by FEM only if a large-displacement formulation is employed.

A three-dimensional DEM analysis is very interesting but evidently difficult because of the heavy computation load. Harada and Gotoh (2006) conducted this type of analysis on the transportation of river bed grains, taking simply into account the water effects. They employed 9,350 grains.

(a) Initial configuration prior to shaking.
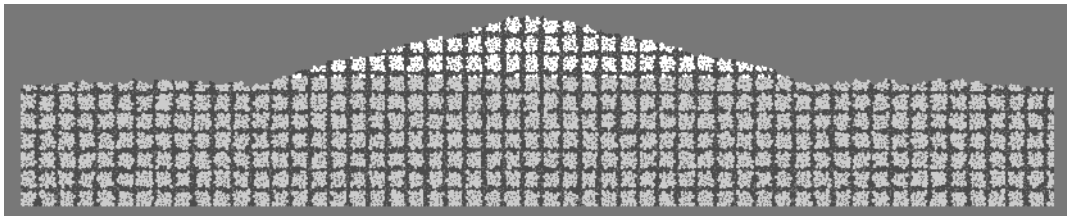
(b) Confguration after subsidence into liquefied subsoil.
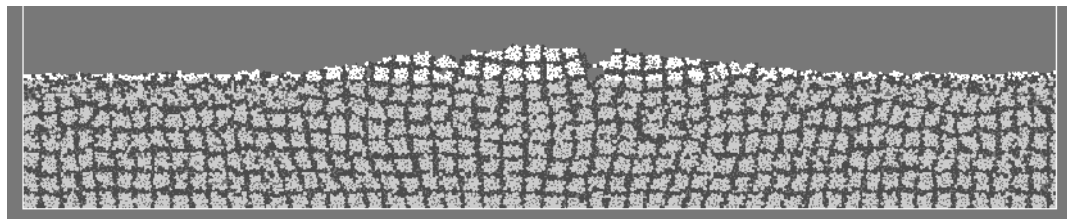

Fig. 11.30 DEM calculation on subsidence of embankment into liquefied subsoil
(Honda and Towhata, 2006)

List of References in Chapter 11

Cundall, P.A. (1971) A computer model for simulating progressive, large-scale movements in blocky rock systems, Proc. Symp. Int. Soc. Rock Mech., Nancy, p. II-8.

Cundall, P.A. and Strack, O.D.L. (1979) A discrete numerical model for granular assemblies, Geotech., Vol. 29, No. 1, pp. 47–65.

Deresiewicz, H. (1958a) Mechanics of granular matter, Advances in Applied Mechanics, Academic Press, New York, pp. 233–306.

Deresiewicz, H. (1958b) Stress–strain relations for a simple model of a granular medium, J. Appl. Mech., Vol. 25, pp. 402–406.

Fukutake, K. and Matsuoka, H. (1989) A unified law for dilatancy under multi-directional simple shearing, Proc. JSCE, No. 412/III-12, pp. 240–248 (in Japanese).

Hakuno, M. and Tarumi, Y. (1988) A granular assembly simulation for the seismic liquefaction, Struct. Eng. / Earthq. Eng., Vol. 5, No. 2 (Proc. JSCE, No.398/I-10), pp. 333–342.

Harada, E. and Gotoh, H. (2006) Numerical simulation of sediment sorting in sheetflow regime by 3D granular material model, Proc. JSCE B, Vol. 62, No. 1, pp. 128–138 (in Japanese).

Hardin, B.O. and Drnevich, V.P. (1972) Shear modulus and damping in soils design equation and curves, Proc. ASCE, Vol. 98, SM7, pp. 667–692.

Hill, R. (1983) The mathematical theory of plasticity, The Oxford Engineering Science Series, pp. 14–69 (first edition in 1950).

Hinokio, M., Nakai, T., Hoshikawa, T. and Yoshida, H. (2001) Dilatancy characteristics and anisotropy of sand under monotonic and cyclic loading, Soils Found., Vol. 41, No. 3, pp. 107-124.

Honda, T. and Towhata, I. (2006) Factors influencing ground deformation of river dike due to liquefaction by distinct element analysis, Proceedings of IS-Yamaguchi 06 on Geomechanics and Geotechniques of Particulate Media, Ube, Yamaguchi, Japan, pp. 225–232.

Iai, S., Matsunaga, Y. and Kameoka, T. (1992a) Strain space plasticity model for cyclic mobility, Soils Found., Vol. 32, No. 2, pp. 1–15.

Iai, S., Matsunaga, Y. and Kameoka, T. (1992b) Analysis of undrained cyclic behavior of sand under anisotropic consolidation, Soils Found., Vol. 32, No. 2, pp. 16–20.

Ishihara, K. and Towhata, I. (1982) Dynamic response analysis of level ground based on the effective stress method, Soil Mechanics – Transient and Cyclic Loads, Wiley, New York, pp. 133–172.

Ishihara, K. and Towhata, I. (1983) Sand response to cyclic rotation of principal stress directions as induced by wave loads, Soils Found., Vol. 23, No. 4, pp. 11–26.

Iwashita, K. and Oda, M. (1998) Rolling resistance at contacts in simulation of shear band development by DEM, J. Eng. Mech., ASCE, Vol. 124, No. 3, pp. 285–292.

Jennings, P.C. (1964) Periodic response of a general yielding structure, Proc. ASCE, Vol. 90, EM2, pp. 131–166.

Kanatani, M., Kawai, T. and Tochigi, H. (2001) Prediction method on deformation behavior of caisson-type seawalls covered with armored embankment on man-made islands during earthquakes, Soils Found., Vol. 41, No. 6, pp. 79–96.

Kawai, T. and Takeuchi, N. (1981) A discrete method of limit analysis with simplified elements, Proc. 1st Int. Conf. Computing in Civil Eng., pp. 27–42.

Kondner, R.L. (1963) A hyperbolic stress–strain response: Cohesive soils, Proc. ASCE, Vol. 89, SM1, pp. 115–143.

Kondner, R.L. and Zelasko, J.S. (1963) A hyperbolic stress–strain formulation for sands, Proc. 2nd Pan-American Conf. Soil Mech. Found. Eng., Vol.I, pp. 289–324.

Martin, G.R., Finn, W.D.L. and Seed, H.B. (1975) Fundamental of liquefaction under cyclic loading, Proc. ASCE, Vol. 101, GT5, pp. 423–38.

Masing, G. (1926) Eigenspannungen und Verfestigung beim Messing, Proc. 2nd Int. Cong. Applied Mechanics, pp. 332–335.

Mroz, Z., Norris, V.A. and Zienkievicz, O.C. (1978) An anisotropic hardening model for soils and its application to cyclic loading, Int. J. Nume. Anal. Methods Geomech., Vol. 2, pp. 203–221.

Nakase, H. (1999) A simulation study on liquefaction using DEM, Mechanics of Granular Materials, an Introduction, ed. M. Oda and K. Iwashita, publ. A.A.Balkema, The Netherlands, pp. 183–187.

Nishimura, S. and Towhata, I. (2004) A three-dimensional stress–strain model of sand undergoing cyclic rotation of principal stress axes, Soils Found., Vol. 44, No. 2, pp. 103–116.

Pradhan, T.B.S., Tatsuoka, F. and Sato, Y. (1989) Experimental stress–dilatancy relations of sand subjected to cyclic loading, Soils Found., Vol.2 9, No. 1, pp. 45-64.

Shahnazari, H. and Towhata, I. (2002) Torsion shear tests on cyclic stress–dilatancy relationship of sand, Soils Found., Vol. 42, No. 1, pp. 105-119.

Towhata, I. and Ishihara, K. (1985) Modelling soil behaviour under principal stress axes rotation, Proc. of 5th International Conference on Numerical Methods in Geomechanics, Nagoya, Japan, Vol. 1, pp. 523–530.